Green Chemistry

Probing Laser-induced Structural Transformation of Lignin into Few-layer Graphene

Journal:	*Green Chemistry*
Manuscript ID	GC-ART-09-2023-003603.R2
Article Type:	Paper
Date Submitted by the Author:	02-Mar-2024
Complete List of Authors:	Zhang, Hanwen; University of Missouri, Chemical and Biomedical Department Li, Qianwei; University of Missouri, Chemical and Biomedical Engineering Hammond, Karl ; University of Missouri, Chemical and Biomedical Engineering He, Xiaoqing; University of Missouri, Electron Microscopy Core Facilities Lin, Jian; University of Missouri, Mechanical and Aerospace Engineering Wan, Caixia; University of Missouri, Chemical and Biomedical Engineering

Probing Laser-induced Structural Transformation of Lignin into Few-layer Graphene

Hanwen Zhang [a], *Qianwei Li* [a], *Karl D. Hammond* [a], *Xiaoqing He* [b, c], *Jian Lin* [b], *Caixia Wan* [a, *]

[a] Department of Chemical and Biomedical Engineering, University of Missouri, Columbia 65211, USA

[b] Department of Mechanical and Aerospace Engineering, University of Missouri, Columbia, Missouri, USA

[c] Electron Microscopy Core Facilities, University of Missouri, Columbia, Missouri, USA

[*] Corresponding author: Phone: +1 573 884 7882; Fax: +1 573 884 5650; E-mail: wanca@missouri.edu

Abstract

Laser induced graphene (LIG) is a versatile form of graphene materials synthesized through direct laser writing (DLW) onto a carbon-rich precursor. Lignin is a promising natural precursor for LIG. However, the lack of understanding of the relationship between lignin chemistry and LIG properties limits the effective utilization of lignin. Herein, we aim to understand the structural evolution of lignin into few-layer graphene during direct laser writing via the combined experimental investigation and reactive force field molecular dynamics (MD) simulation. Strong correlations are found between structural features of lignin and LIG characteristics, especially the sheet resistance (electrical conductivity) and defects in graphene domains. Specifically, higher molecular weight lignin demonstrates a superior propensity for generating the graphitic structure in the turbostratic matrix of LIG. This phenomenon leads to better graphene quality in terms of morphological continuity, conductivity, and graphene domains. The glass transition temperature (T_g) of fractionated lignin was identified to have the

strongest linear correlation with both sheet resistance and defects density in LIG. Additionally, the MD simulations shed light on the role of closely positioned carbon atoms in the initial substrate, highlighting their facilitative effect on the formation of large graphene domains. The proposed LIG formation pathway offers a new avenue for lignin refinery, facilitating an efficient production of graphene materials from renewable resources.

Keywords: laser-induced graphene, direct laser writing, lignin, advanced carbon material

Introduction

Lignin is the second most abundant natural polymer on Earth after cellulose. In pulping mill and biorefinery operation facilities, lignin is generated as a major byproduct, and 50–70 million tons of lignin are produced annually from those facilities.[1-3] Converting lignin into high-value-added materials rather than burning lignin as a low-quality solid fuel for heat and power applications is expected to increase the profitability and sustainability of biorefineries and pulp mills.[4] Lignin has been explored for use in industrially important products, such as adsorbents,[5] carbonaceous materials,[2] and hydrogels.[6] Expanding the spectrum of lignin-derived products will not only further promote value-added use of lignin but also introduce a new class of sustainable bioproducts (especially built on lignin's aromatic structures) for various industrial applications. Among various lignin-derived bioproducts, graphene-based materials have received extensive interests given their extraordinary properties regarding electrical, thermal, and mechanical behaviors, making it one of the most promising platform nanomaterials.[7] Laser-induced graphene (LIG) is one emerging graphene-based materials with high value and multifunctionality, which has been extensively studied in the past decade. The formation of LIG is realized via direct laser writing (DLW), during which precursors can be rapidly converted into 3D graphene materials (i.e., LIG) under ambient conditions.[8-10] This process is distinct from conventional techniques for

synthesis of graphene materials, as it involves one step, is relatively fast, and is chemical-free, rather than involving a series of lengthy and tedious chemical reactions.[11, 12] Lignin and lignin-containing substrates are highly promising precursors to making quality LIG with a reduced carbon footprint and high sustainability.[10, 13] Lignin-derived LIG has been explored for versatile applications including wearable electronics,[14-16] chemical sensors,[17, 18] soft robotics,[19] and energy storage devices.[20]

Polymeric structure of lignin comprises abundant aromatic units, which makes lignin a preferential precursor for producing graphene and other advanced carbon materials. However, lignin possesses different interlinkages, subunits, and molecular weight distributions, depending on the botanical origin of lignin and/or its processing conditions.[21] The complex and heterogeneous nature of lignin thus imposes technical barriers to effectively upgrade it into advanced carbon and other materials. Therefore, research efforts have been made to probe the relationship between lignin structure/chemistry and target carbon products.

Prior studies reported that lignin structure has pronounced effects on its behavior during thermal treatment and the properties of the resultant carbon.[22-25] For porous carbon production via pyrolysis coupled with activation, lignin with low molecular weight is thought to be labile to carbonization, leading to more porous graphitic materials, as it has more free volume, more end groups, and higher chain mobility.[23, 24] Oxygen-containing functional groups easily decompose into small molecules (e.g., CO_2, H_2O) by thermal degradation, which can in turn act as physical activation agents, resulting in highly porous carbon.[24, 26] Lignin subunits and interunit linkages also affect lignin carbonization efficiency. Prior studies also showed that hardwood lignin can be more efficiently carbonized via pyrolysis than softwood.[22, 27] It should be noted that DLW, typically using a CO_2 laser, induces reaction conditions distinct from conventional thermal

conditions, which could lead to different reaction mechanisms involved in lignin carbonization and graphitization. However, there is a lack of fundamental understanding of how lignin chemistry can affect LIG characteristics. To effectively convert lignin by laser writing, it is necessary to take a deeper look at the interaction of lignin with the laser, as well as the relationship between lignin source/structure and LIG properties. Reactive force field (ReaxFF) molecular dynamics (MD) simulation is an effective method to study the mechanisms of lignin decomposition at the atomic level. It has been widely used to study chemical evolution and product structure during the lignin pyrolysis process and carbon fiber formation.[28, 29] In terms of LIG formation, researchers have found that high temperatures and pressures locally induced by a laser are the driving forces of the rearrangement of carbon atoms.[30] Dong et al.[30] found that polyimide with repeating units can be converted into graphene at 2400 K and 3 GPa. Vashisth et al.[31] found that under the same conditions, polybenzimidazole resulted in the highest LIG yields over four other polymers (i.e., polyimide, polyetherimide, polycarbonate, and polyether ether ketone) because of the absence of oxygen from the polymer backbone. However, to date, no studies have been done to study the mechanism of LIG formation from lignin at the atomic level using MD simulation.

Herein, we aim to probe how lignin structural features can define LIG properties. Lignin fractions with different molecular weights are obtained from the fractionation of kraft lignin using an acetone-water mixture and used for LIG synthesis. LIG properties are found to be linked to lignin characteristics based on a series of characterization techniques. MD simulations further provide valuable insight into the mechanisms of LIG formation from lignin especially with different molecular weights. This work not only reveals the relationships between lignin chemistry and LIG properties, but also offers guidance in preparing suitable lignin precursors for

carbon-based materials with desired characteristics.

Experimental section

Lignin Fractionation. Softwood kraft lignin was fractionated with an acetone-water mixture according to the scheme in Figure S1.[32] Briefly, 100 g of kraft lignin was dissolved in 1000 mL of 60 vol% acetone-water mixture. After 2 h of stirring, deionized (DI) water was added to the acetone solution to reduce the acetone concentration from 60% to 55%. After another 60 min moderate stirring, the precipitated lignin (KL55) was vacuum filtered. The filtrate was further diluted with water to reduce the acetone concentration to 50%. After another 60 min of moderate stirring, the precipitated lignin (KL50) was separated by vacuum filtration. Another two kraft lignin fractions, KL40 and KL25, were collected following the same procedure for KL50 by adding water to respective filtrates to adjust the acetone concentrations to 40% and 25%, respectively. The soluble lignin in 25% acetone (KL0) was precipitated by removing the acetone from the mixture by vacuum. All the kraft lignin fractions were vacuum dried at 50 °C and stored in a desiccator prior to further use.

LIG preparation. Lignin was first made into a film substrate prior to laser writing. The film was prepared by mixing a lignin solution and polyvinyl alcohol (PVA) at 1:1 (v/v) at room temperature for 5 min. The lignin solution was prepared by fully dissolving 1 g of an individual lignin fraction into 10 ml of 2% (w/w) NaOH solution. PVA (M_w =146 000–186 000 Da) solution was made by dissolving 1 g of PVA to 10 ml of deionized water. The homogenous mixture was poured into a petri dish to form a film with ~9 cm in diameter (about 0.2 mm thick) and then dried at 40 °C in an incubator. The dried film was cut into different dimensions for DLW.

A CO_2 laser (VLS 3.50 universal laser system, 10.6 μm wavelength, 30 W power limit, ~ 27 inch/s maximum scanning speed) was used to irradiate the lignin/PVA films under ambient

conditions for LIG formation. The image density was set as 5 and the pulse per inch (PPI) set as 1000. The laser beam was focused at 2 mm above an irradiated substrate. The laser scanning speed was fixed at 3% of the upper speed limit. Three laser power levels (i.e., 10%, 12%, and 14% of the upper laser power limit) were used for scribing. The LIG samples were denoted as KLx-LIG-y, where KLx stands for individual kraft lignin fractions (i.e., KL0, KL25, KL40, KL50, KL55) and y for individual power levels in percentage (i.e., 10%, 12%, 14%).

Lignin characterization. GPC measurements were performed on an Agilent 1200 series high performance liquid chromatography (HPLC) system (Agilent Technologies, Palo Alto, CA) equipped with an ultraviolet (UV) detector and an Agilent PLgel 5 μm MIXED-D column (300 × 7.5 mm). The column temperature was maintained at 35 °C. Tetrahydrofuran (THF) with a flow rate of 1 mL/min was used as the mobile phase. The GPC column was calibrated using polystyrene standards with molecular weights ranging from 266 to 66 000 g/mol. The UV wavelength was 254 nm. All the lignin samples were acetylated for complete dissolution of lignin in THF prior to the GPC analysis.[33] DSC analysis was performed on a Thermal Analysis (TA) DSC-Q10 under a nitrogen flow of 20 mL/min. About 6 mg of sample were placed into a tared DSC aluminum pan and the weight of the sample was accurately recorded. Two-dimensional Heteronuclear Single Quantum Coherence nuclear magnetic resonance (2D HSQC NMR) analysis was conducted on a 600 MHz Bruker AVANCE III spectrometer. Each lignin sample (~80 mg) was dissolved in 0.6 mL of DMSO-d_6. A Bruker-supplied pulse sequence named hsqcetgp was used, and the number of scans was 32. After Fourier transformation, phase correction, and baseline correction, the spectra were calibrated with respect to the solvent signals (δ_C/δ_H: 39.5/2.49 ppm).[33] The assignments of the signals of lignin substructures are listed in Table S1, as described in prior studies.[34-36] Semiquantification of

lignin substructures was performed according to prior studies using the G_2 signals as internal standard.[37] ^{31}P NMR analysis was performed on a 300 MHz Bruker AVANCE II+ spectrometer, and 128 scans were used to ensure a good signal-to-noise ratio.[38] Bruker's Topspin 4.1.4 was used for the data processing and signal integration of NMR spectra.

LIG characterization. Sheet resistances (R_s) of LIG was measured on a four-probe bridge resistivity system (Keithley 2400 Series SourceMeter®). Three LIG samples (each with 6.4 × 6.4 mm) prepared under the same conditions were used for R_s measurement, and the average R_s values were reported. Raman spectra were collected on a Renishaw inVia™ Raman spectrometer with a wavelength of 633 nm. X-ray photoelectron spectroscopy (XPS) analysis was carried out on a Thermoscientific Nesxa Photo Electron Spectroscopy system with a monochromatic Al Kα X-ray source (72W, 400 μm diameter slot). XPS survey spectra were obtained with the pass energy at 200 pe and the step size at 0.50 eV. High-resolution spectra were acquired with the pass energy at 50 pe and the step size at 0.10 eV. The spectra were corrected by using the predominant C–C peak as a reference (284.4 eV). The deconvolution of high-resolution peaks was performed using the XPSpeak 4.1 software. Shirley backgrounds were used for all peak fitting purposes. Scanning electron microscope (SEM) images were collected on an FEI Quanta 600 FEG Environmental SEM. All the samples were sputter-coated with 10 nm of platinum before collecting SEM images. High resolution transmission electron microscopy (HRTEM) images were acquired on a Thermofisher Spectra 300 TEM operated at 300 kV. The LIG was scraped off from the substrate, dispersed in ethanol and subsequently 5 mL of dispersion was dropped onto a TEM grid and air-dried for TEM imaging. Powder X-ray diffraction analysis was performed as reported in our prior work.[8] XRD patterns were acquired on a Bruker X8 Prospector diffractometer equipped with an Apex II CCD area detector (Bruker

AXS, Madison, WI, USA). LIG powder scaped from the film substrates was transferred to polyimide tubes and used for XRD analysis. The diffraction patterns were recorded with a step size of 0.02°, spanning 2θ from 20° to 50°.

Simulation methods. Two lignin models (i.e., G2 and G6, shown in Figure S2a&b) and the initial simulation system were generated using Atlas (Molydyn, Bristol, UK). Table S2 lists the specifications of the two starting simulation systems. Different numbers of molecules were put into different systems to make the total atoms of both systems similar. After the initial equilibrium performed by Atlas under the DREIDING force field at 300 K, the systems were switched to the ReaxFF and equilibrated at 300 K for 25 picoseconds (ps) using a Nosé–Hoover thermostat with a time constant of 25 femtoseconds (fs), followed by additional equilibrium process at 300 K and 1 atm for 100 ps using a Nosé–Hoover thermostat and barostat with time constants of 25 and 250 fs, respectively. The time step was set to 0.25 fs and periodic boundary conditions were applied throughout the simulation. Two different configurations were collected in the last 50 ps for each system as the starting configuration for the high temperature reaction simulation and the data were averaged over the two trajectories. The ReaxFF used in this work has been previously used to simulate the shock wave impact of nitramine RDX and the LIG formation from polyimide.[30, 39] After reaching thermal equilibrium, a Nosé–Hoover thermostat with a time constant of 25 fs was used to simulate the LIG formation reaction at high temperature. As shown in Figure S2c, the temperature was increased from 300 to 3000 K at a speed of 200 K/ps. Then, the temperature was kept at 3000 K for 600 ps and finally cooled down to 300 K for another 600 ps.

Results and discussions

Chemistry of refined lignin. Aqueous acetone was used to refine kraft lignin into five

fractions with varying properties since the solubility of lignin in acetone can be tuned by water addition.[32]. Table 1 shows the characteristics of the lignin fractions. Both weight-average molecular weight (M_w) and number-average molecular weight (M_n) showed declining trends when the acetone concentration decreased. Meanwhile, decreasing acetone concentration had a more profound effect on M_w than M_n. The high dispersity (M_w/M_n) of KL55 indicated that a significant amount of low-molecular-weight lignin was precipitated out along with high-molecular-weight lignin even when the acetone concentration was high. On the other hand, low-molecular-weight lignin fractions, such as KL0 and KL25, showed a narrow-ranged molecular weight distribution, as reflected by a lower dispersity compared to high-molecular-weight lignin fractions. KL55 possessed the highest M_w (9800 g/mol) among the five fractions, which was more than five-fold higher than the lowest one (KL0, M_w 1700 g/mol). With such a wide range of M_w, the prepared lignin fractions can serve as good model precursors to study the relationship between lignin and LIG properties. Glass transition temperatures (T_g) of lignin fractions shared a similar trend to molecular weights due to polymer chain mobility/stiffness (Figure S3). The highest T_g was about 203.2 °C from KL55, and the lowest T_g was 126.9 °C from KL0. It was previously found that polymers with higher T_g are more favorable for LIG formation because they are less susceptible to ablation by the laser.[40] Thus, both molecular weight and T_g were used primarily to probe their effects on LIG properties.

2D HSQC NMR was used to study the detailed chemical structure of the lignin fractions (Figure 1a&b&S4a–c). In the aromatic region, only guaiacyl (G) units were observed in all fractions, which is consistent with other softwood lignin.[41, 42] Five major lignin interlinkages, including β-O-4′, β-β′, β-5′, secoisolariciresinol, and stilbene were found in all the samples and were semi-quantified on the basis of G_2 signals (Table 1). The contents of β-O-4′, β-β′, and β-5′

interlinkages contents showed clear positive correlation with molecular weights. On the other hand, the abundance of stilbene and secoisolariciresinol structures did not show a clear correlation with lignin molecular weight, with KL0 possessing the lowest stilbene content and the highest secoisolariciresinol content. Those major interlinkages along with aromatic rings should play the key roles in the formation of carbon radicals by laser irradiation, which in turn react with each other to form graphene matrix.[30]

Since only one methoxy group was attached on the aromatic ring in the G unit, side reactions can happen on the position C5 of the aromatic ring during kraft pulping, which may contribute to a more condensed structure in the softwood kraft lignin.[34] Although HSQC NMR cannot directly detect the condensed structure of aryl-O-aryl (4-O-5′, F1 in Figure 1) and biphenyl (5-5′, F2 in Figure 1), the upfield-shifted G_2 signals and downfield-shifted G_6 signals confirmed that such condensed structures exist in all the kraft lignin fractions.[36] We also used ^{31}P NMR to study the contents of condensed and non-condensed phenolic hydroxyl groups in the lignin fractions with the highest and lowest molecular weights (i.e., KL55 and KL0) (Figure S5). The contents of the condensed (C_5-subsituted) structure were evaluated by comparing the content of condensed and non-condensed phenolic hydroxyl groups based on signal intensity. KL55 showed 59% condensed structure, while KL0 only had 39%. This suggests that the high-molecular-weight lignin has a higher content of condensed structures than low-molecular-weight lignin. Such unique structural differences can also affect the LIG formation process, as further discussed below.

LIG characteristics. The morphology of LIG obtained at 12% laser power was first investigated (Figure 2). At low magnification, all LIG exhibited striped patterns resulting from the line-by-line laser beam trajectory. LIG prepared from the lowest molecular weight lignin

fraction (KL0) showed a flake-like but less porous structure aligned in the same direction as the laser bean movement (Figure 2a&f). When lignin with higher molecular weights was used, the LIG showed more distinct interconnected porous structures, effectively acting as bridges between the LIG flakes (Figures 2f–2j). This is presumably because low-molecular-weight lignin tends to form more gaseous products which released from the substrate, leading to a more fragmented structure within the LIG matrix.

The LIG formed from all the kraft lignin fractions was highly electrically conductive. Figure 3 shows the R_s of LIGs prepared at different laser powers. At 12% laser power, the LIG from KL0 showed the highest R_s of 23 Ω/square among all the five lignin fractions. This could be due to the poor interconnections in the LIG matrix, as discussed above. In contrast, LIG prepared from high-molecular-weight lignin exhibited improved conductivity, with the lowest R_s of 13.8 Ω/square coming from KL55. Besides a better interconnected pore structure, larger graphene domains with less defects in LIG from high-molecular-weight lignin can also contribute to the observed higher electrical conductivity, as discussed below.

Two more laser power levels (i.e., 10% and 14%) were also used to study the power effect on the conductivity of LIG. Similar to LIG formed from other substrates,[9, 43] the higher laser power (below the threshold causing the detrimental effects) can induce more graphitization of the precursor. Although the trend of R_s at three power levels was similar, the difference in the R_s between KL0-LIG and KL55-LIG obtained at the lowest laser power level (10%) is more significant than for LIG made at the highest laser power level (14%) (R_s ratio of KL0-LIG to KL55-LIG of 1.75 vs. 1.49). Plausibly, this is because a high laser power level masked the effects of different lignin structures. Since the present work is focused on studying the lignin properties and LIG properties, an intermediate laser power level (i.e., 12%) was chosen as a

representative level in the following sections.

Raman spectroscopy is a useful tool for analyzing graphene-basedmaterials.[44] Three major peaks (i.e., G peak at ~1580 cm^{-1}, D peak at ~1360 cm^{-1}, and 2D peak at ~2700 cm^{-1}) can be found in the Raman spectra of LIG prepared from all the lignin fractions (Figure 3b). The G peak is from the E_{2g} phonons of carbon sp^2 atoms, and the D peak is a result of K-point phonons of A_{1g} symmetry, which is induced by defects in the structure.[45] The peak area ratio of the D peak to the G peak (i.e., I_D/I_G) serves as a good estimator of the quality of graphene-based materials. The 2D peak, originating from second-order zone-boundary phonons, is characteristic of graphene and graphene-related materials.[45] The peak area ratios for LIG generated from different lignin fractions are plotted in Figure 3c. LIG prepared from the high-molecular-weight lignin showed lower I_D/I_G ratios than that from low-molecular-weight lignin, indicating fewer defects, with the fewest defects in KL55-devired LIG (corresponding to the lowest I_D/I_G of 0.376). This is consistent with the sheet resistivity data, as defects in the graphene generally decrease the conductivity.

To further study how the molecular weight of lignin affects the LIG properties, LIG derived from the lignin fractions with the highest and lowest molecular weights (i.e., KL55 and KL0, respectively) was analyzed in more detail. XPS was used to study the chemical composition and carbon chemical states on the surface of the LIG samples. The two most abundant elements in the LIG matrix were C and O (Figure S6a), suggesting the presence of oxygen-containing functional groups or oxygen-induced defects within the LIG structure, which is consistent with the Raman results in Figure 3b. Sodium was also detected in small amounts, which originated from NaOH used for dissolving the kraft lignin during the film preparation process.[9, 46] The carbon content of KL55-LIG-12, at 63.83%, is substantially higher compared to

46.26% in KL0-LIG-12, suggesting a more thorough graphitization process in KL55 than in KL0. High-resolution carbon XPS spectra of both LIG samples indicate a significant difference in carbon chemical states (Figure S6b&c). The C1s peak can be deconvoluted into 7 peaks, which represent different carbon chemical states.[47] The percentage of sp^2-hybridized carbon is higher in KL55-LIG-12 with 54.3% compared to 43.2% in KL0-LIG-12, indicating a greater involvement of carbon atoms in forming ordered graphene structures in KL55-LIG-12 compared to KL0-LIG-12. On the other hand, the higher concentration of C/O bonds (e.g., C–O, C=O) in KL0-LIG-12 (32.5%), in comparison to KL55-LIG-12 (21.2%), suggests more oxygen functionalization on its surface, which can potentially disrupt the electrical conductivity by interfering with the graphene lattice's conductive pathways.

HRTEM images show ultrastructure in KL55-LIG-12 and KL0-LIG-12 (Figure 4). Amorphous carbon and turbostratic few-layer graphene structures were observed in both LIG samples (Figure 4c and 4d), which can be attributed to the intrinsic dynamics of LIG synthesis and the nature of the precursor. During the laser irradiation, decoupling and rearrangement of carbon atoms happen in a very short time. The rapid heating and cooling does not allow for a uniform or directional alignment of the newly formed graphene structures. Thus, the few-layer graphene structures are randomly oriented within the LIG matrix. Aliphatic carbon, with a less ordered structure, may require higher laser energy to be converted into an ordered few-layer graphene structure, compared to aromatic carbons. In other words, while aromatic carbons may successfully transition into graphene structures, aliphatic carbons may undergo partial transformation under the same condition, resulting in the formation of amorphous carbon.[48]

LIG-KL55-12 exhibited a higher content of few-layer graphene structures than LIG-KL0-12. The large area of irregular patterns in Figure 4c indicates a significant amount of amorphous

carbon in LIG-KL0-12. The insets of Figures 4c and 4d show the patterns obtained from the areas marked in red squares after fast Fourier transform (FFT). Two clear rings were observed in the FFT pattern from KL55-LIG-12 as a result of graphene characteristic plane distances (i.e., (002) and (100) planes). Multiple bright Bragg spots were observed in the (002) diffraction ring, confirming the turbostratic feature in KL55-LIG-12 with few-layer graphene structure orienting toward different directions. On the other hand, only blurred rings were observed in the FFT image from KL0-LIG-12, confirming the limited graphitization of KL0 under the same laser conditions.

XRD pattern of LIG-KL55-12 confirms the formation of few-layer graphene structures (Figure S7). The peak observed at 2θ=26.0° is attributed to the (002) plane of LIG, which suggests the presence of few-layer graphene structures with the interlayer spacing of around 0.34 nm. The peak at 2θ=43.1° typically corresponds to the (100) plane of graphitic materials, which reflects the ordered arrangement of carbon atoms within the individual graphene layers.

Correlation between lignin structure and LIG characteristics. Linear regression analysis was used to explore the correlation between lignin properties and LIG properties. As one of the most distinctive characteristics, the molecular weights of lignin were first employed to study its effects on the properties of LIG. Strong linear correlations were found between lignin molecular weights and R_s of LIG. As shown in Figures 5a and 5b, R_s of LIG made from three laser power levels, especially at two higher ones (12% and 14%), were well correlated with average molecular weight. The strongest correlation between R_s and Mn was observed at 14% power level. We also found that M_n had a stronger linear correlation with R_s than M_w. Such correlations can provide guidance in the selection and modification of lignin precursors for LIG by controlling the molecular weights of lignin precursors. The relative abundance of lignin

interlinkages also showed good linear correlation with R_s ($R^2 = 0.884$) at 14% laser power (Figure 5c). When more lignin interlinkages exist in the precursor, more aromatic rings are more likely to be close to each other, allowing more graphene rings to form during the fast bond cleavage and formation processes.

The glass transition temperature, T_g, is a fundamental parameter in the characterization of lignin, serving as a comprehensive indicator of its structural attributes. This pivotal parameter is not only solely influenced by the molecular weight of lignin but also by its chemical composition and the extent of branching within the lignin structure. As such, T_g emerges as a representative measure that encapsulates the intricate characteristics of lignin's molecular makeup and has been considered as an important factor in the production of lignin-derived carbon fiber and epoxy resin.[49, 50] Strong linear correlations were found between T_g and the sheet resistance at all three power levels (Figure 5d). Near-perfect linear correlation ($R^2 = 0.995$) was found at the highest laser power level (14%), while the other two power levels also showed outstanding correlations (i.e., $R^2 = 0.910$ and $R^2 = 0.927$). The regression analysis between the five individual lignin interlinkages and the sheet resistance of the LIG formed at 14% were also studied (Figures S8a–e) since different lignin substructures may undergo quite different reaction pathways toward the formation of LIG. The lignin interlinkages A, B, and C showed substantial influences on the R_s ($R^2 = 0.844$–0.959). On the other hand, lignin interlinkages D and E did not show linear correlation with sheet resistance. Interestingly, the total relative abundance of B and C showed a significantly higher R^2 (0.978) (Figure S8f), indicating that the ring structure in the lignin side chains (e.g., benzodioxane structures in B) can contribute significantly to the graphene formation, leading to LIG with good conductivity.

The correlation between the lignin characteristics and LIG Raman band ratios at 12%

laser power (i.e., I_D/I_G) was also investigated (Figure S9). All the lignin characteristics show good linear correlation with I_D/I_G. Notably, the correlation of M_n and T_g with I_D/I_G are particulary strong (R^2 = 0.955 and 0.945, respectively). In contrast, M_w and relative abundances of interlinkages had lower linear correlations with I_D/I_G (R^2 =0.881 and 0.858, respectively). These trends are consistent with the correlations observed with R_s. This further suggests that M_n and T_g can be used as parameters to predict graphene properties.

LIG has turbostratic structures featuring mixtures of graphitic and amorphous domains.[51] The graphitic domains should play a more important role in the overall performance of LIG. Highly branched lignin with high molecular weight and condensed structure can be considered a better precursor than that with low molecular weight and linear structure for the formation of few-layer graphene structure. The better linear correlations between M_n/M_w and R_s and between M_n/M_w and I_D/I_G suggest that molecular weight is a more significant determinant for LIG characteristics than lignin interlinkage content. These findings provide insights into the relationship between the lignin structure and LIG properties. Future research could involve employing lignin with similar molecular weight but different structure to further understand the structural transformation of lignin molecules to LIG.

ReaxFF MD simulation of LIG formation from lignin. We studied LIG formation from lignin at the atomic level via MD simulations with the ReaxFF force field.[39, 52] Two lignin models were used, namely, G2 with 320 g/mol molecular weight and G6 with 1104 g/mol molecular weight (Table S2). Figure S10 shows the pressure changes during the simulation. High pressures were generated in both systems as a result of the high temperature (i.e., 3000 K) and small molecule formation (e.g., gaseous products, light hydrocarbons). After reaching the peak pressure, the pressure in both systems gradually decreased because of the repolymerization of

small molecules, which forms the graphene structure. Figures 6a and 6b show the ring structure evolution in the largest cluster during the simulations. In both simulated systems, the total number of rings dropped at the beginning of the heating, as the aromatic rings decomposed at high temperature. During the annealing process, more six-membered rings were observed, indicating the formation of traditional honeycomb graphene structures. In the meantime, significant amounts of five- and seven-membered rings were also observed in both systems, leaving defects in the LIG matrix. The percentages of different types of rings of the final products (named as G2-LIG and G6-LIG) from G2 and G6 are compared in Figure 6c, which can be used to evaluate the concentration of defects. G6-LIG possessed a higher percentage of 6-membered rings (~61%) than that of G2-LIG (52%), indicating that graphene with few defects was formed from G6 under these reaction conditions. These results are consistent with the experimental data from the fractionated lignin as revealed in the Raman spectra (Figures 3b and 3c). Figure 6d compares the radial distribution function (rdf) of carbon atoms in the final systems from two models. Both systems exhibit four distinct peaks, each corresponding to the specific distances between carbon atoms in a graphitic structure (as shown in the inset of Figure 6d). Notably, in G6-LIG, the peak heights for all four distances surpass those observed in G2-LIG. This observation suggests that G6-LIG exhibits a greater degree of graphitic structure formation compared to G2-LIG. To investigate the possible reasons for such phenomena, we compared the locations of aromatic carbon atoms and aliphatic carbon atoms in the final LIG structures. For example, Figure 7a shows the snapshot of the all-carbon system at the end of the simulation from G2. Figures 7b and 7c are from the same viewpoint but with only aromatic carbons and aliphatic carbons shown, respectively. In Figure 7b, only a few carbon rings were observed, which suggests an extensive aromatic ring cleavage and carbon atom rearrangement. However, large

clusters consisting of long aliphatic chains and carbon rings were formed by the aromatic groups, which participated in the formation of the backbone of the final graphene sheet. On the other hand, although some of the aliphatic carbons were involved in the formation of the ring structure, most of these carbon atoms were isolated in the graphene structure, as revealed by the single aliphatic carbon atoms in Figure 7c. We conclude that aliphatic carbon in lignin does not facilitate the formation of large graphene sheets. Similar phenomena were also observed in the final structure of G6 (Figure S11). Based on the simulation results, we propose that in the initial system, carbon atoms which are close to each other, especially those were already in a ring structure, are more likely to form large carbon clusters that can serve as a graphene backbone. G6 can be considered to be three G2 molecules connected to each other by β-O-4′ interlinkages. Although the substructures and carbon atoms content of G2 and G6 are similar, the extra lignin interlinkage allows more G units close to each other, potentially forming an intertwined structures and facilitating the formation of large honeycomb graphene structures.

Proposed LIG formation pathways and mechanisms. The LIG formation mechanisms involve both photochemical and photothermal effects.[48, 53, 54] Given the low photon energy generated by the CO_2 laser, which operates at a relatively long wavelength (10.6 μm), the photochemical effects are expected to be minimal.[48, 55] Thus, only photothermal effects were taken into consideration. In brief, the laser irradiation creates a localized temperature ramp on the surface of the substrate, which promotes bond cleavage of C–C, C–O, and C–H in both aromatic and aliphatic regions in lignin as well as in PVA which served as a binder in the lignin film.[48] Subsequently, C, O and H atoms undergo reorganization and recombination, leading to the formation of volatile products and a few-layer graphene structure. The released gaseous products contributed to the porous morphology of LIG, and they became ionized to form a plasma plume,

which prevented further heat penetration and generated a localized region of high temperature.[54] Due to the high oxygen content and the long aliphatic chain structure of PVA, PVA is more likely to be converted into amorphous carbon and gaseous products such as CO and CO_2, rather than few-layer graphene structures. In contrast, the abundant aromatic backbone of lignin allows more carbon atoms to repolymerize into graphene. Since such a laser-induced conversion happens in a very short timeframe, we propose that the molecule geometry plays a crucial role in determining the performance of different lignin fractions. For instance, carbon atoms in the large and branched polymer chains in KL55 are more likely to recombine into graphene. Additionally, as revealed by the ^{31}P NMR data (Figure S5), the highly condensed structure of KL55 makes it more conducive to the ring-closure reactions during the graphitization process. The resulting turbostratic graphene structure and well-defined ring structure endow LIG with fewer defects and high electrical conductivity. On the other hand, due to the smaller molecular size/shorter polymer chain of KL0, the size of the layered graphene is constrained, resulting in the formation of more amorphous carbon and less graphene domains. Additionally, more carbon atoms in this lignin precursor are exposed to the long PVA chain. Consequently, the combination of carbon atoms in lignin and the large number of neighboring H and O atoms in PVA tend to generate more gaseous products rather than facilitating carbon atom rearrangement.

Conclusions

This work revealed the relationship between structural features of lignin-based precursors and LIG characteristics. Good linear correlations were observed between the main lignin attributes (especially M_n and T_g) and key LIG characteristics such as R_s and defects (I_D/I_G ratio). LIG prepared from lignin with high molecular weight was found to have a noticeable 3D porous structure, higher electrical conductivity, and better graphene domains. ReaxFF MD simulations

of LIG formation from lignin models with varying molecular weights aligned consistently with experimental findings. This underscored an approach to guide the optimization of lignin precursors through computational modeling. Furthermore, these simulations shed light on a possible mechanism underlying LIG formation and its properties. The findings extend beyond the realm of high-quality LIG production from lignin, offering valuable perspectives for its applications based on other aromatic precursors. Overall, this work facilitates lignin upgrading with high values and contributes significantly to sustainable material development and green chemistry. It offers a new avenue to producing LIG and other advanced carbon materials from rationally selected/refined lignin and related materials.

ASSOCIATED CONTENT

Supporting Information

Additional experimental section including schematic diagram of the kraft lignin fractionation process; detailed specification and additional results of the MD simulations; additional linear correlation between lignin characteristics and LIG properties; additional characterization data including DSC curves, 2D NMR spectra, XPS spectra, and XRD

AUTHOR INFORMATION

Corresponding Author

* Phone: (573) 884-7882. Fax: (573) 884-5650. E-mail: wanca@missouri.edu.

ORCID

Hanwen Zhang: 0000-0003-0766-1816

Karl Hammond: 0000-0002-5424-8752

Jian Lin: 0000-0002-4675-2529

Caixia Wan: 0000-0001-5490-7490

Declaration of Competing Interest

The authors declare that they have no competing interests.

ACKNOWLEDGEMENTS

This work was supported by the National Science Foundation (Award No. 1933861). The authors thank Domtar Corporation (Fort Mills, South Carolina) for providing kraft lignin. The authors acknowledge the use of electron microscopy core facilities at the University of Missouri.

Figure captions

Figure 1. 2D HSQC NMR spectra of (a) KL0 and (b) KL55. The assignments of signals are listed in Table S1.

Figure 2. SEM images of LIG synthesized from the lignin fractions at 12% laser power. (a, f) K0-LIG-12, (b, g) K25-LIG-12, (c, h) K40-LIG-12, (d, i) K50-LIG-12, and (e, j) K55-LIG-12.

Figure 3. (a) Sheet resistance (Rs) of LIG prepared from the fractionated lignin at different laser powers. (b) Raman spectra of LIG prepared at 12% laser power. (c) Raman peak ratios of LIG prepared at 12% laser power.

Figure 4. TEM images: (a,c) LIG-KL0-12, (b,d) LIG-KL55-12. Insets in (c) and (d) are the FFT images of the area marked in the red squares (scale bar: 10 1/nm).

Figure 5. Correlations of lignin's main characteristics and the sheet resistance (Rs) of LIG at different laser powers. (a) Number average molecular weight (*Mn*) vs. *Rs*, (b) Weight average molecular weight (*Mw*) vs. *Rs*, (c) Relative abundance of five lignin interlinkages vs. *Rs*, and (d) Glass transition temperature (*Tg*) vs. *Rs*.

Figure 6. The count of carbon ring structure in the largest cluster from different starting materials: (a) G2-LIG and (b) G6-LIG. The *y-axes* are the number of rings divided by the number of carbon atoms in the system and times 100, indicating the number of rings can be formed from every 100 carbon atoms. (c) Comparison of the percentage of carbon ring structure in different systems at the end of the simulation. (d) Radial distribution function (rdf) calculation for carbon atoms.

Figure 7. Snapshots of final simulation system with G2 as the initial molecule (carbon atoms only). (a) All carbon atoms, (b) Aromatic carbon atoms only, and (c) Aliphatic carbon atoms only. The blue atoms are the aromatic carbon atoms originating from G2. The red atoms are the aliphatic carbon atoms originating from G2.

Table 1. Characteristics of the lignin fractions.

Sample	Molecular weight distribution*			Relative abundance** (/100Ar)					C5-condensed Phenols (%)
	M_n (g/mol)	M_w (g/mol)	Dispersity	A	B	C	D	E	
KL0	931	1450	1.56	3.49	1.07	0.81	3.32	2.29	39
KL25	1465	2471	1.69	3.52	1.3	1.19	2.52	3.04	-
KL40	2075	4165	2.01	4.00	1.56	1.35	2.33	2.85	-
KL50	2731	7130	2.61	4.85	1.98	1.63	2.39	2.51	-
KL55	2674	9647	3.61	5.83	2.36	1.67	2.31	2.64	59

* M_n: number-average molecular weight. M_w: weight-average molecular weight.

**A: □-O-4′, B: □-5′, C: □-□′, D: Secoisolariciresinol, E: Stilbene.

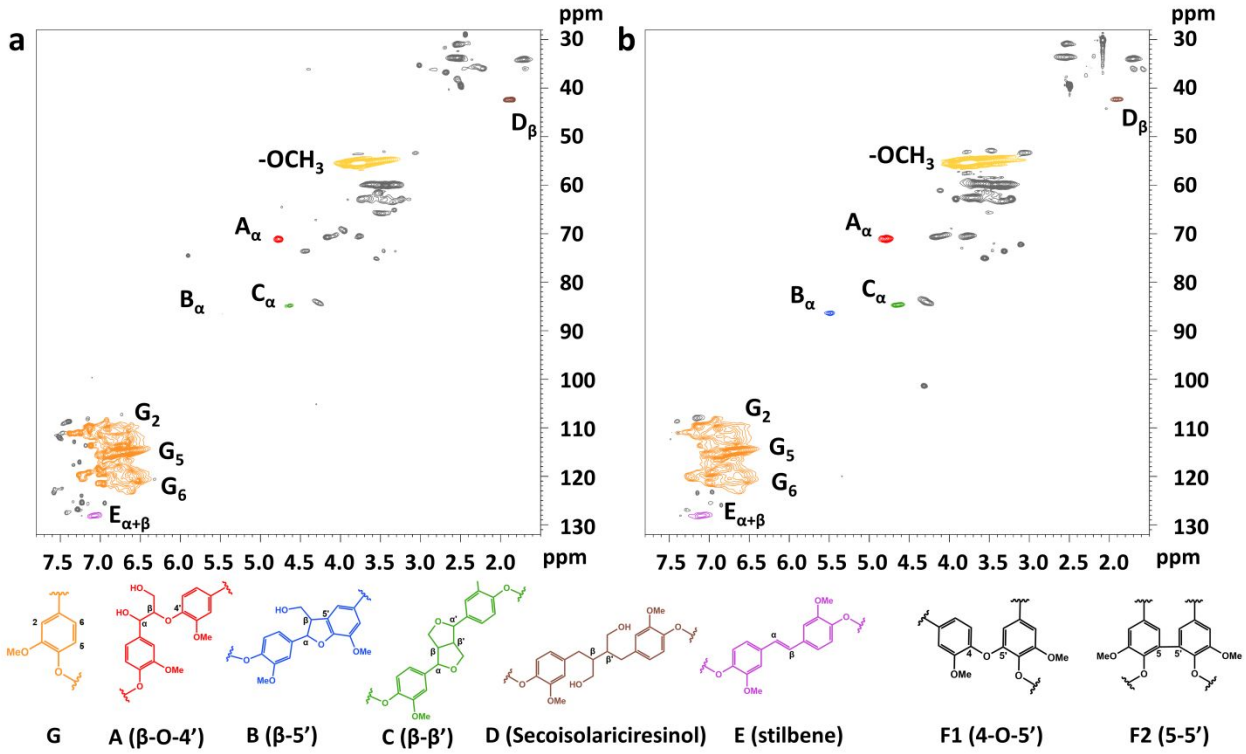

Figure 1. 2D HSQC NMR spectra of (a) KL0 and (b) KL55. The assignments of signals are listed in Table S1.

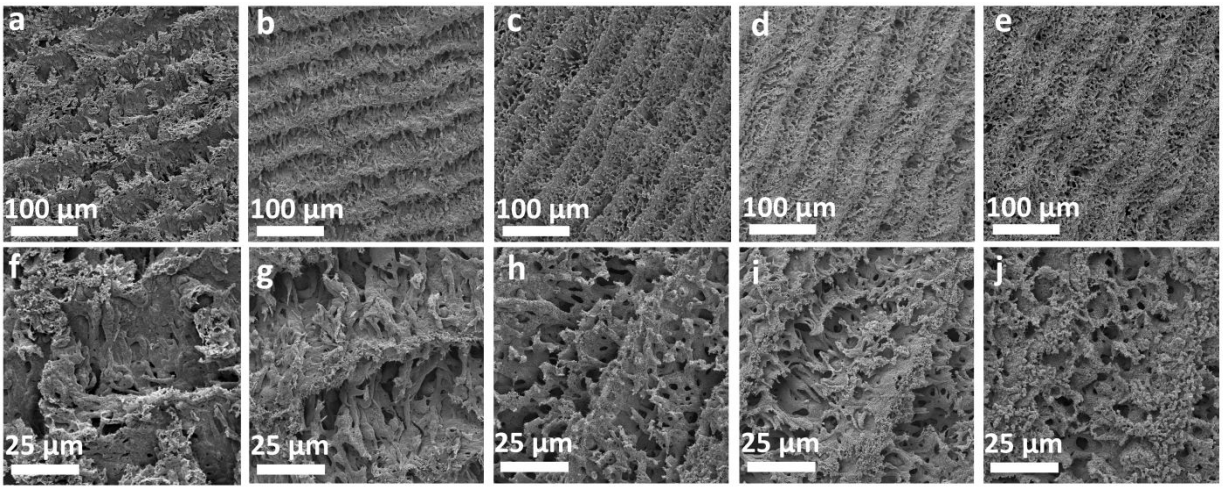

Figure 2. SEM images of LIG synthesized from the lignin fractions at 12% laser power. (a, f) K0-LIG-12, (b, g) K25-LIG-12, (c, h) K40-LIG-12, (d, i) K50-LIG-12, and (e, j) K55-LIG-12.

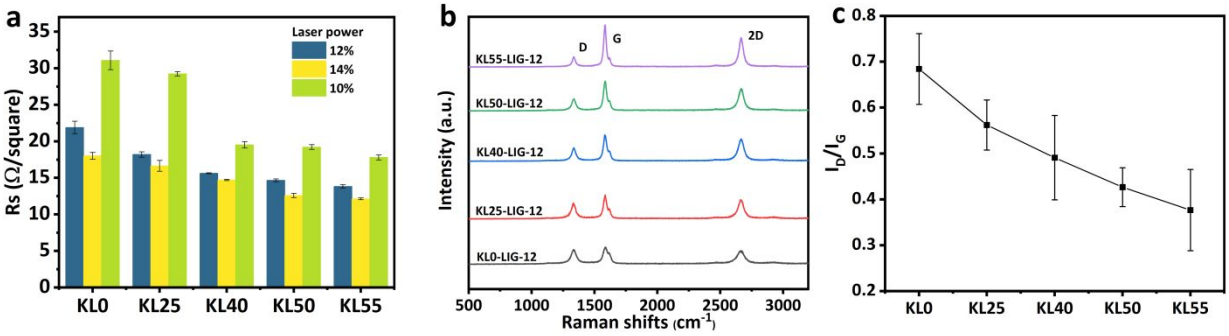

Figure 3. (a) Sheet resistance (Rs) of LIG prepared from the fractionated lignin at different laser powers. (b) Raman spectra of LIG prepared at 12% laser power. (c) Raman peak ratios of LIG prepared at 12% laser power.

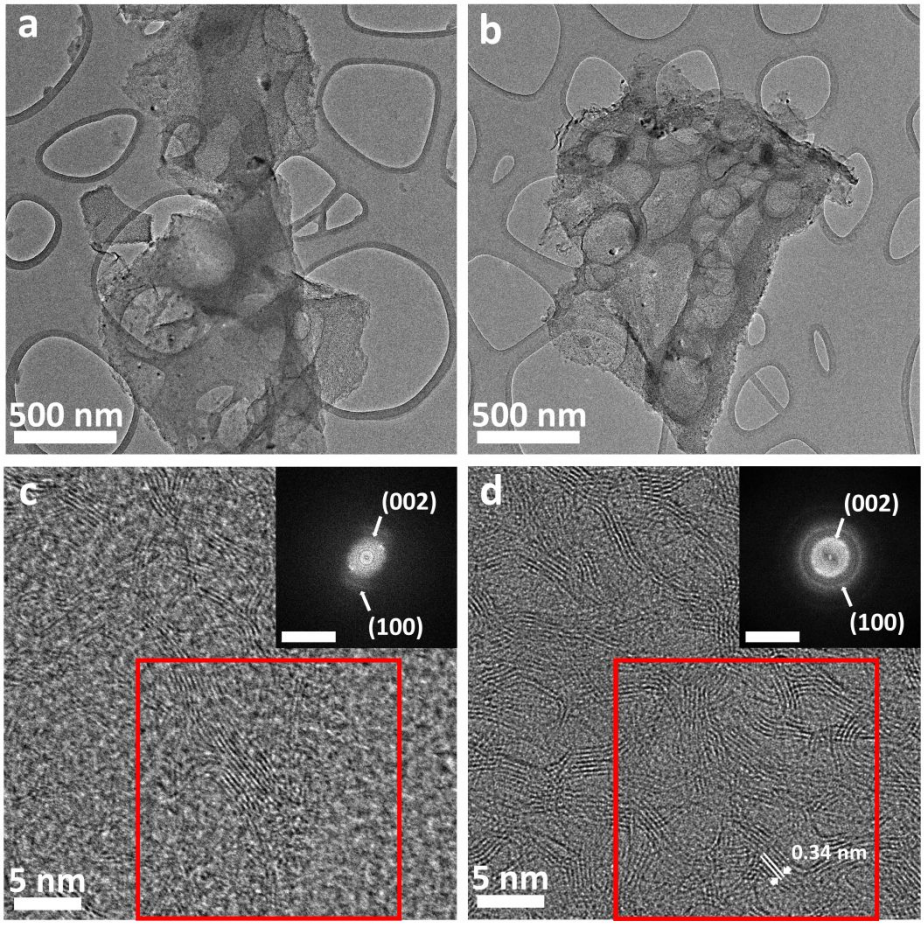

Figure 4. TEM images: (a,c) LIG-KL0-12, (b,d) LIG-KL55-12. Insets in (c) and (d) are the FFT images of the area marked in the red squares (scale bar: 10 1/nm).

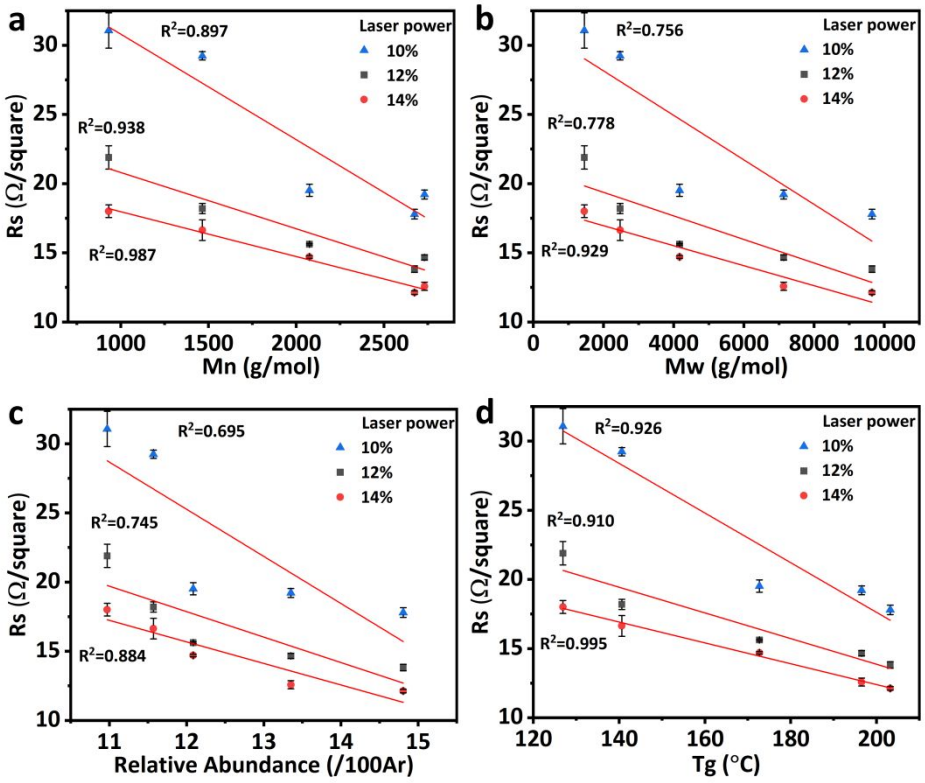

Figure 5. Correlations of lignin's main characteristics and the sheet resistance (Rs) of LIG at different laser powers. (a) Number average molecular weight (M_n) vs. R_s, (b) Weight average molecular weight (M_w) vs. R_s, (c) Relative abundance of five lignin interlinkages vs. R_s, and (d) Glass transition temperature (T_g) vs. R_s.

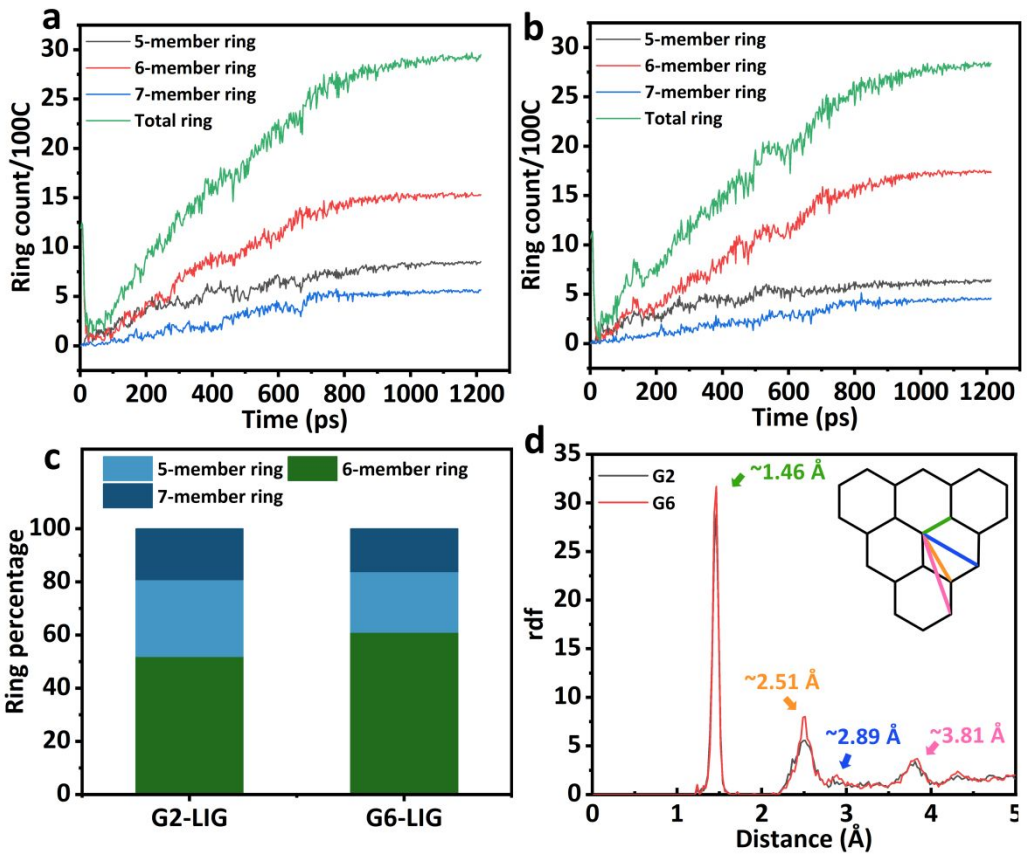

Figure 6. The count of carbon ring structure in the largest cluster from different starting materials: (a) G2-LIG and (b) G6-LIG. The *y*-axes are the number of rings divided by the number of carbon atoms in the system and times 100, indicating the number of rings can be formed from every 100 carbon atoms. (c) Comparison of the percentage of carbon ring structure in different systems at the end of the simulation. (d) Radial distribution function (rdf) calculation for carbon atoms.

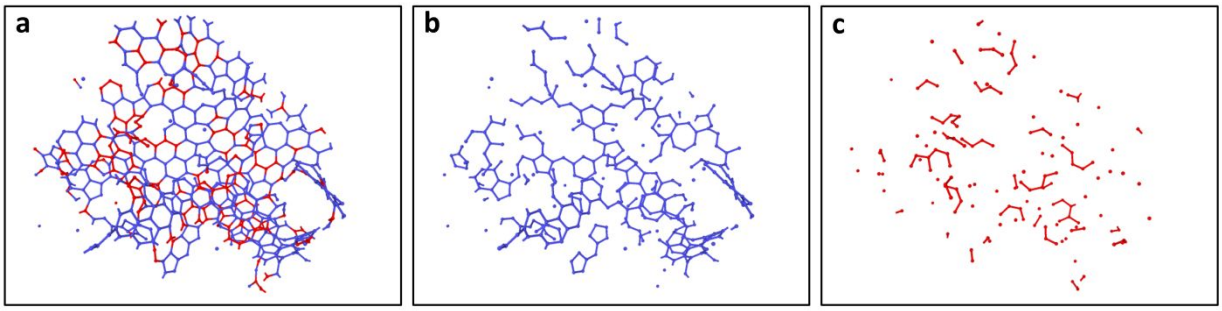

Figure 7. Snapshots of final simulation system with G2 as the initial molecule (carbon atoms only). (a) All carbon atoms, (b) Aromatic carbon atoms only, and (c) Aliphatic carbon atoms only. The blue atoms are the aromatic carbon atoms originating from G2. The red atoms are the aliphatic carbon atoms originating from G2.

References

(1) Saito, T.; Brown, R. H.; Hunt, M. A.; Pickel, D. L.; Pickel, J. M.; Messman, J. M.; Baker, F. S.; Keller, M.; Naskar, A. K. Turning renewable resources into value-added polymer: Development of lignin-based thermoplastic. *Green Chem.* **2012**, *14* (12), 3295-3303.

(2) Zhang, W.; Qiu, X.; Wang, C.; Zhong, L.; Fu, F.; Zhu, J.; Zhang, Z.; Qin, Y.; Yang, D.; Xu, C. C. Lignin derived carbon materials: Current status and future trends. *Carbon Research* **2022**, *1* (1), 14.

(3) Tribot, A.; Amer, G.; Abdou Alio, M.; de Baynast, H.; Delattre, C.; Pons, A.; Mathias, J.-D.; Callois, J.-M.; Vial, C.; Michaud, P.; et al. Wood-lignin: Supply, extraction processes and use as bio-based material. *Eur. Polym. J.* **2019**, *112*, 228-240.

(4) Wang, H.-M.; Yuan, T.-Q.; Song, G.-Y.; Sun, R.-C. Advanced and versatile lignin-derived biodegradable composite film materials toward a sustainable world. *Green Chem.* **2021**, *23* (11), 3790-3817.

(5) Supanchaiyamat, N.; Jetsrisuparb, K.; Knijnenburg, J. T. N.; Tsang, D. C. W.; Hunt, A. J. Lignin materials for adsorption: Current trend, perspectives and opportunities. *Bioresour. Technol.* **2019**, *272*, 570-581.

(6) Meng, Y.; Lu, J.; Cheng, Y.; Li, Q.; Wang, H. Lignin-based hydrogels: A review of preparation, properties, and application. *Int. J. Biol. Macromol.* **2019**, *135*, 1006-1019.

(7) Choi, W.; Lahiri, I.; Seelaboyina, R.; Kang, Y. S. Synthesis of graphene and its applications: A review. *Crit Rev Solid State* **2010**, *35* (1), 52-71.

(8) Zhang, H.; Sun, Y.; Li, Q.; Wan, C. Upgrading lignocellulose to porous graphene enabled by deep eutectic solvent pretreatment: Insights into the role of lignin and pseudo-lignin. *ACS Sustainable Chem. Eng.* **2022**, *10* (35), 11501-11511.

(9) Zhang, W.; Lei, Y.; Ming, F.; Jiang, Q.; Costa, P. M. F. J.; Alshareef, H. N. Lignin laser lithography: A direct-write method for fabricating 3d graphene electrodes for microsupercapacitors. *Adv. Energy Mater.* **2018**, *8* (27), 1801840.

(10) Ye, R.; Chyan, Y.; Zhang, J.; Li, Y.; Han, X.; Kittrell, C.; Tour, J. M. Laser-induced graphene formation on wood. *Adv. Mater.* **2017**, *29* (37), 1702211.

(11) Chen, Z.; Ren, W.; Gao, L.; Liu, B.; Pei, S.; Cheng, H.-M. Three-dimensional flexible

and conductive interconnected graphene networks grown by chemical vapour deposition. *Nat. Mater.* **2011**, *10* (6), 424-428.

(12) Estevez, L.; Kelarakis, A.; Gong, Q.; Da'as, E. H.; Giannelis, E. P. Multifunctional graphene/platinum/nafion hybrids via ice templating. *J. Am. Chem. Soc.* **2011**, *133* (16), 6122-6125.

(13) Kulyk, B.; Silva, B. F. R.; Carvalho, A. F.; Silvestre, S.; Fernandes, A. J. S.; Martins, R.; Fortunato, E.; Costa, F. M. Laser-induced graphene from paper for mechanical sensing. *ACS Appl. Mater. Interfaces* **2021**, *13* (8), 10210-10221.

(14) Sun, B.; McCay, R. N.; Goswami, S.; Xu, Y.; Zhang, C.; Ling, Y.; Lin, J.; Yan, Z. Gas-permeable, multifunctional on-skin electronics based on laser-induced porous graphene and sugar-templated elastomer sponges. *Adv. Mater.* **2018**, *30* (50), e1804327.

(15) Tao, L.-Q.; Tian, H.; Liu, Y.; Ju, Z.-Y.; Pang, Y.; Chen, Y.-Q.; Wang, D.-Y.; Tian, X.-G.; Yan, J.-C.; Deng, N.-Q.; et al. An intelligent artificial throat with sound-sensing ability based on laser induced graphene. *Nat. Commun.* **2017**, *8* (1), 14579.

(16) Zhao, N.; Zhang, H.; Yang, S.; Sun, Y.; Zhao, G.; Fan, W.; Yan, Z.; Lin, J.; Wan, C. Direct induction of porous graphene from mechanically strong and waterproof biopaper for on-chip multifunctional flexible electronics. *Small* **2023**, 2300242.

(17) Nayak, P.; Kurra, N.; Xia, C.; Alshareef, H. N. Highly efficient laser scribed graphene electrodes for on-chip electrochemical sensing applications. *Adv. Electron. Mater.* **2016**, *2* (10), 1600185.

(18) Yang, Y.; Song, Y.; Bo, X.; Min, J.; Pak, O. S.; Zhu, L.; Wang, M.; Tu, J.; Kogan, A.; Zhang, H.; et al. A laser-engraved wearable sensor for sensitive detection of uric acid and tyrosine in sweat. *Nat. Biotechnol.* **2020**, *38* (2), 217-224.

(19) Ling, Y.; Pang, W.; Li, X.; Goswami, S.; Xu, Z.; Stroman, D.; Liu, Y.; Fei, Q.; Xu, Y.; Zhao, G.; et al. Laser-induced graphene for electrothermally controlled, mechanically guided, 3d assembly and human–soft actuators interaction. *Advanced Materials* **2020**, *32* (17), 1908475.

(20) Peng, Z.; Ye, R.; Mann, J. A.; Zakhidov, D.; Li, Y.; Smalley, P. R.; Lin, J.; Tour, J. M. Flexible boron-doped laser-induced graphene microsupercapacitors. *ACS Nano* **2015**, *9* (6), 5868-5875.

(21) Sadeghifar, H.; Ragauskas, A. Perspective on technical lignin fractionation. *ACS Sustainable Chem. Eng.* **2020**, *8* (22), 8086-8101.

(22) Li, W.; Zhang, Y.; Das, L.; Wang, Y.; Li, M.; Wanninayake, N.; Pu, Y.; Kim, D. Y.; Cheng, Y.-T.; Ragauskas, A. J.; et al. Linking lignin source with structural and electrochemical properties of lignin-derived carbon materials. *RSC Advances* **2018**, *8* (68), 38721-38732.

(23) Qin, H.; Jian, R.; Bai, J.; Tang, J.; Zhou, Y.; Zhu, B.; Zhao, D.; Ni, Z.; Wang, L.; Liu, W.; et al. Influence of molecular weight on structure and catalytic characteristics of ordered mesoporous carbon derived from lignin. *ACS Omega* **2018**, *3* (1), 1350-1356.

(24) Jeon, J. W.; Zhang, L. B.; Lutkenhaus, J. L.; Laskar, D. D.; Lemmon, J. P.; Choi, D.; Nandasiri, M. I.; Hashmi, A.; Xu, J.; Motkuri, R. K.; et al. Controlling porosity in lignin-derived nanoporous carbon for supercapacitor applications. *Chemsuschem* **2015**, *8* (3), 428-432.

(25) Ho, H. C.; Nguyen, N. A.; Meek, K. M.; Alonso, D. M.; Hakim, S. H.; Naskar, A. K. A solvent-free synthesis of lignin-derived renewable carbon with tunable porosity for supercapacitor electrodes. *ChemSusChem* **2018**, *11* (17), 2953-2959.

(26) Saha, D.; Li, Y.; Bi, Z.; Chen, J.; Keum, J. K.; Hensley, D. K.; Grappe, H. A.; Meyer, H. M.; Dai, S.; Paranthaman, M. P.; et al. Studies on supercapacitor electrode material from activated lignin-derived mesoporous carbon. *Langmuir* **2014**, *30* (3), 900-910.
(27) Zhou, S.; Xue, Y.; Sharma, A.; Bai, X. Lignin valorization through thermochemical conversion: Comparison of hardwood, softwood and herbaceous lignin. *ACS Sustainable Chem. Eng.* **2016**, *4* (12), 6608-6617.
(28) Zhang, T.; Li, X.; Guo, L.; Guo, X. Reaction mechanisms in pyrolysis of hardwood, softwood, and kraft lignin revealed by reaxff md simulations. *Energy & Fuels* **2019**, *33* (11), 11210-11225.
(29) Zhu, J.; Gao, Z.; Kowalik, M.; Joshi, K.; Ashraf, C. M.; Arefev, M. I.; Schwab, Y.; Bumgardner, C.; Brown, K.; Burden, D. E.; et al. Unveiling carbon ring structure formation mechanisms in polyacrylonitrile-derived carbon fibers. *ACS Appl. Mater. Interfaces* **2019**, *11* (45), 42288-42297.
(30) Dong, Y.; Rismiller, S. C.; Lin, J. Molecular dynamic simulation of layered graphene clusters formation from polyimides under extreme conditions. *Carbon* **2016**, *104*, 47-55.
(31) Vashisth, A.; Kowalik, M.; Gerringer, J. C.; Ashraf, C.; van Duin, A. C. T.; Green, M. J. Reaxff simulations of laser-induced graphene (lig) formation for multifunctional polymer nanocomposites. *ACS Appl. Nano Mater.* **2020**, *3* (2), 1881-1890.
(32) Sadeghifar, H.; Wells, T.; Le, R. K.; Sadeghifar, F.; Yuan, J. S.; Jonas Ragauskas, A. Fractionation of organosolv lignin using acetone:Water and properties of the obtained fractions. *ACS Sustainable Chem. Eng.* **2016**, *5* (1), 580-587.
(33) Chen, Z.; Bai, X.; A, L.; Zhang, H.; Wan, C. Insights into structural changes of lignin toward tailored properties during deep eutectic solvent pretreatment. *ACS Sustainable Chem. Eng.* **2020**, *8* (26), 9783-9793.
(34) Crestini, C.; Lange, H.; Sette, M.; Argyropoulos, D. S. On the structure of softwood kraft lignin. *Green Chem.* **2017**, *19* (17), 4104-4121.
(35) Zhao, C.; Huang, J.; Yang, L.; Yue, F.; Lu, F. Revealing structural differences between alkaline and kraft lignins by hsqc nmr. *Ind. Eng. Chem. Res.* **2019**, *58* (14), 5707-5714.
(36) Balakshin, M. Y.; Capanema, E. A.; Chen; Gracz, H. S. Elucidation of the structures of residual and dissolved pine kraft lignins using an hmqc nmr technique. *J. Agric. Food. Chem.* **2003**, *51* (21), 6116-6127.
(37) Sette, M.; Wechselberger, R.; Crestini, C. Elucidation of lignin structure by quantitative 2d nmr. *Chemistry – A European Journal* **2011**, *17* (34), 9529-9535.
(38) Meng, X.; Crestini, C.; Ben, H.; Hao, N.; Pu, Y.; Ragauskas, A. J.; Argyropoulos, D. S. Determination of hydroxyl groups in biorefinery resources via quantitative 31p nmr spectroscopy. *Nature Protocols* **2019**, *14* (9), 2627-2647.
(39) Strachan, A.; van Duin, A. C. T.; Chakraborty, D.; Dasgupta, S.; Goddard, W. A. Shock waves in high-energy materials: The initial chemical events in nitramine rdx. *Phys. Rev. Lett.* **2003**, *91* (9), 098301.
(40) Chyan, Y.; Ye, R.; Li, Y.; Singh, S. P.; Arnusch, C. J.; Tour, J. M. Laser-induced graphene by multiple lasing: Toward electronics on cloth, paper, and food. *ACS Nano* **2018**, *12* (3), 2176-2183.
(41) Li, W.; Zhang, Y.; Das, L.; Wang, Y.; Li, M.; Wanninayake, N.; Pu, Y.; Kim, D. Y.; Cheng, Y. T.; Ragauskas, A. J.; et al. Linking lignin source with structural and electrochemical properties of lignin-derived carbon materials. *RSC Adv.* **2018**, *8* (68), 38721-38732.

(42) Hu, Z.; Du, X.; Liu, J.; Chang, H.-m.; Jameel, H. Structural characterization of pine kraft lignin: Biochoice lignin vs indulin at. *J. Wood Chem. Technol.* **2016**, *36* (6), 432-446.
(43) Lin, J.; Peng, Z.; Liu, Y.; Ruiz-Zepeda, F.; Ye, R.; Samuel, E. L.; Yacaman, M. J.; Yakobson, B. I.; Tour, J. M. Laser-induced porous graphene films from commercial polymers. *Nat. Commun.* **2014**, *5*, 5714.
(44) Wu, J. B.; Lin, M. L.; Cong, X.; Liu, H. N.; Tan, P. H. Raman spectroscopy of graphene-based materials and its applications in related devices. *Chem. Soc. Rev.* **2018**, *47* (5), 1822-1873.
(45) Ferrari, A. C.; Meyer, J. C.; Scardaci, V.; Casiraghi, C.; Lazzeri, M.; Mauri, F.; Piscanec, S.; Jiang, D.; Novoselov, K. S.; Roth, S.; et al. Raman spectrum of graphene and graphene layers. *Phys. Rev. Lett.* **2006**, *97* (18), 187401.
(46) Strauss, V.; Marsh, K.; Kowal, M. D.; El-Kady, M.; Kaner, R. B. A simple route to porous graphene from carbon nanodots for supercapacitor applications. *Adv. Mater.* **2018**, *30* (8).
(47) Smith, M.; Scudiero, L.; Espinal, J.; McEwen, J.-S.; Garcia-Perez, M. Improving the deconvolution and interpretation of xps spectra from chars by ab initio calculations. *Carbon* **2016**, *110*, 155-171.
(48) C. Claro, P. I.; Pinheiro, T.; Silvestre, S. L.; Marques, A. C.; Coelho, J.; Marconcini, J. M.; Fortunato, E.; C. Mattoso, L. H.; Martins, R. Sustainable carbon sources for green laser-induced graphene: A perspective on fundamental principles, applications, and challenges. *Appl. Phys. Rev.* **2022**, *9* (4), 041305.
(49) Li, Q.; Xie, S.; Serem, W. K.; Naik, M. T.; Liu, L.; Yuan, J. S. Quality carbon fibers from fractionated lignin. *Green Chem.* **2017**, *19* (7), 1628-1634.
(50) Gioia, C.; Lo Re, G.; Lawoko, M.; Berglund, L. Tunable thermosetting epoxies based on fractionated and well-characterized lignins. *J. Am. Chem. Soc.* **2018**, *140* (11), 4054-4061.
(51) Nayak, P.; Jiang, Q.; Kurra, N.; Wang, X.; Buttner, U.; Alshareef, H. N. Monolithic laser scribed graphene scaffolds with atomic layer deposited platinum for the hydrogen evolution reaction. *J. Mater. Chem. A* **2017**, *5* (38), 20422-20427.
(52) Aktulga, H. M.; Fogarty, J. C.; Pandit, S. A.; Grama, A. Y. Parallel reactive molecular dynamics: Numerical methods and algorithmic techniques. *Parallel Computing* **2012**, *38* (4), 245-259.
(53) Schaaf, P. *Laser processing of materials: Fundamentals, applications and developments*; Springer Science & Business Media, 2010.
(54) Devi, M.; Rawat, S.; Sharma, S. A comprehensive review of the pyrolysis process: From carbon nanomaterial synthesis to waste treatment. *Oxford Open Materials Science* **2021**, *1* (1), itab014.
(55) Chatani, S.; Kloxin, C. J.; Bowman, C. N. The power of light in polymer science: Photochemical processes to manipulate polymer formation, structure, and properties. *Polym. Chem.* **2014**, *5* (7), 2187-2201.